Water-vapour variability within a convective boundary-layer assessed by large-eddy simulations and IHOP_2002 observations

By F. COUVREUX[1]*, F. GUICHARD[1], J.-L. REDELSPERGER[1], C. KIEMLE[3], V. MASSON[1], J.-P. LAFORE[1] and C. FLAMANT[2]

[1]*Centre National de Recherches Météorologiques–Météo-France and Centre National de Recherche Scientifique, France*
[2]*Institut Pierre Simon Laplace/Service d'Aéronomie, France*
[3]*Deutsche Zentrum für Luft- und Raumfahrt/Institut für Physik der Atmosphäre, Germany*

SUMMARY

This study presents a comprehensive analysis of the variability of water vapour in a growing convective boundary-layer (CBL) over land, highlighting the complex links between advection, convective activity and moisture heterogeneity in the boundary layer. A Large-eddy Simulation (LES) is designed, based on observations, and validated, using an independent data-set collected during the International H_2O Project (IHOP_2002) field-experiment. Ample information about the moisture distribution in space and time, as well as other important CBL parameters are acquired by mesonet stations, balloon soundings, instruments on-board two aircraft and the DLR airborne water-vapour differential-absorption lidar. Because it can deliver two-dimensional cross-sections at high spatial resolution (140 m horizontal, 200 m vertical), the airborne lidar offers valuable insights of small-scale moisture-variability throughout the CBL. The LES is able to reproduce the development of the CBL in the morning and early afternoon, as assessed by comparisons of simulated mean profiles of key meteorological variables with sounding data. Simulated profiles of the variance of water-vapour mixing-ratio were found to be in good agreement with the lidar-derived counterparts. Finally, probability-density functions of potential temperature, vertical velocity and water-vapour mixing-ratio calculated from the LES show great consistency with those derived from aircraft *in situ* measurements in the middle of the CBL. Downdraughts entrained from above the CBL are governing the scale of moisture variability. Characteristic length-scales are found to be larger for water-vapour mixing-ratio than for temperature

The observed water-vapour variability exhibits contributions from different scales. The influence of the mesoscale (larger than LES domain size, i.e. 10 km) on the smaller-scale variability is assessed using LES and observations. The small-scale variability of water vapour is found to be important and to be driven by the dynamics of the CBL. Both lidar observations and LES evidence that dry downdraughts entrained from above the CBL are governing the scale of moisture variability. Characteristic length-scales are found to be larger for water-vapour mixing-ratio than for temperature and vertical velocity. In particular, intrusions of drier free-troposphere air from above the growing CBL impose a marked negative skewness on the water-vapour distribution within it, both as observed and in the simulation.

KEYWORDS: Heterogeneities   High-resolution simulations   Humidity   Lidar data

1. INTRODUCTION

Water vapour is important in several major areas in the atmospheric sciences, on scales from turbulence to synoptic-scale systems, and including cloud formation and maintenance, radiation and climate. Numerous studies have underlined the importance of the moisture field for convection. Crook (1996), for example, showed that the thermodynamic structure (both temperature and moisture) of the boundary layer (BL) is crucial for the development of deep convection. Moreover, convective boundary layer (CBL) circulations are responsible for moisture variations that can still be quite large (e.g., Weckwerth *et al.* 1996). A common manifestation of such BL heterogeneities takes the form of fair weather cumuli, which arise when and where thermals bring sufficiently moist air from the lower BL to its lifting condensation level (Stull 1985, Wilde *et al.* 1985). Weckwerth (2000) showed how small-scale water-vapour variability could also affect the determination of whether or not deep convection will be initiated through its impact on atmospheric stability.

* Corresponding author: Fleur Couvreux, CNRM/GAME (CNRS and Météo-France), 42 avenue Coriolis, 31057 Toulouse Cedex, France. e-mail: fleur.couvreux@meteo.fr

A few studies have provided partial description of the water-vapour distribution in the BL, based exclusively on observations. For instance, Crum and Stull (1987) and Weckwerth *et al.* (1996) derived distributions from aircraft *in situ* data and radiosondes. Their results suggest a complex structure for the field of water-vapour mixing-ratio (r_v), which is not properly represented by a simple Gaussian distribution. Weckwerth *et al.* (1996) reported a range of fluctuations on the order of 1.5 to 2.5 g kg^{-1} (for a mean value around 15 g kg^{-1}) for r_v in the mixed layer; it further increased in the entrainment zone. They noted a negative skewness of r_v within the CBL. In both studies, the focus was on the quasi-stationary BL of the afternoon. Another approach is the use of Large-eddy Simulations (LES) which, by resolving the most energetic structures, manage to reproduce most features observed in the CBL (e.g., Moeng 1984; Mason 1989; Schmidt and Schumann 1989). Once validated, LES can be further used in order to understand the mechanisms leading to the existence of these structures and test sensitivities to external parameters (e.g., temperature-inversion strength). However, whereas the mean structures and fluctuations of the temperature and vertical-velocity fields in the CBL have been extensively studied with LES, less attention has been devoted to the humidity field. Some inferences can be drawn from scalar analysis (Moeng and Wyngaard, 1984; Jonker *et al.* 1999) even though the water vapour is not a real passive scalar.

At the present time, our knowledge of the water-vapour distribution is still insufficient to understand its impact on the formation of clouds. Radiosondes, the traditional method for measuring water vapour, are usually launched twice per day from sites separated by several hundreds of kilometres: they undersample severely the time- and space-scales of water-vapour variability. In the last two decades however, remote sensing instruments have been developed to measure water vapour with accurate temporal- and spatial-resolutions (see Weckwerth *et al.* (1999) for a review). In particular, a recent field-experiment, the International H$_2$O Project (IHOP_2002), was aimed at obtaining an improved characterization of the time-varying three-dimensional water-vapour field and evaluating its utility in improving the understanding and prediction of convective processes. IHOP_2002 took place over the US Southern Great Plains (SGP) from 13 May to 25 June 2002, and brought together many of the existing operational and new state-of-the-art research water-vapour sensors including remote sensing instruments—see Flamant *et al.* (2003) and Weckwerth *et al.* (2004) for more details.

The case-study presented here focuses on the growing CBL documented in the vicinity of Homestead, Oklahoma (see Fig. 1), 14 June 2002. On this day, three aircraft, the University of Wyoming King Air (UWKA), the Naval Research Laboratory P-3 (P-3) and the Deutsches Zentrum für Luft- und Raumfahrt (DLR) Falcon (the P-3 and Falcon being equipped with differential-absorption lidars—DIALs) as well as a number of other mobile platforms (among which the Mobile Cross-chain Loran Atmospheric Sounding System—MCLASS—and the Mobile GPS/Loran Atmospheric Sounding System—MGLASS) converged on Homestead between 1200 and 1900 UTC (0700–1400 Local Time; UTC = LT + 5). The P-3 and the UWKA operated in the CBL whereas the Falcon flew higher for downward-looking DIAL operation. In addition, Homestead hosted an Integrated Surface and Sounding System (ISS). In the area of interest to this study (see Fig. 1(b)), a total of twenty-seven soundings were acquired with ISS, MCLASS and MGLASS that day. Furthermore, Integrated Surface Flux Facility (ISFF) sites in Booker, Texas (ISFF-1, located in a fallow) and in Elmwood, Oklahoma (ISFF-2, in a grassland environment) provided surface-flux data within a few tens of kilometres from Homestead (Fig. 1(b)).

A LES was designed to complement the analysis of the observations. The approach pursued here aims at addressing three objectives: firstly, to quantitatively assess whether
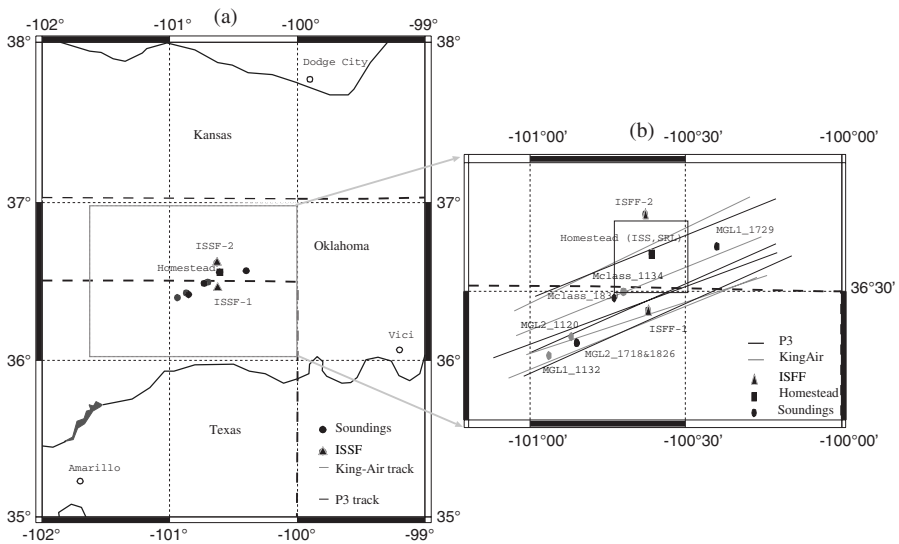
Figure 1. The area of interest, showing observation sites (solid black triangles denote Integrated Surface Flux Facility (ISFF) stations) and aircraft tracks: (a) wider view, showing Kansas, Oklahoma and Texas, USA. Solid light grey circles denote soundings at about 1200 UTC; solid black circles denote soundings at about 1730 UTC; open black circles denote National Weather Service and Atmospheric Radiation Measurement sounding stations (Amarillo, Dodge City and Vici) and the black square denotes the position of Homestead; (b) larger scale map of box in (a) around Homestead, and aircraft tracks on 14 June 2002; grey denotes the track of the UWKA and black the P-3. The black square denotes the location of Homestead and the square box the LES domain.

such a simulation is able to reproduce the observed fluctuations of water vapour in the CBL; secondly, to characterize the ranges and scales of variability of this moisture field, and, thirdly, to explain the mechanisms responsible for such a variability. Note that the environmental conditions required for this IOP operation were optimal for the design of our LES: very few clouds, weak winds in the CBL as well as aloft (i.e. small wind-shear across the CBL top). Numerous and various observations (soundings, aircraft data, lidar data, and surface-flux measurements, for example) are used to design the LES initial and boundary conditions as well as to validate the LES ability to reproduce the development of the CBL in the late morning and early afternoon. This latter stage is a prerequisite before using the LES results for improving our understanding of the processes controlling moisture variability in the CBL.

The outline of the present paper is as follows. Section 2 presents the environmental conditions on 14 June 2002, including the contributions from different scales to the observed moisture-variability. Section 3 briefly describes the set up of the LES. Section 4 presents the simulated and observed properties of CBL along with LES sensitivity analyses. Section 5 analyses the water-vapour fluctuations, both those simulated and those observed using aircraft *in situ* data, lidar data and soundings. Discussion and conclusions are given in the last section.

2. ENVIRONMENTAL CONDITIONS AND MOISTURE VARIABILITY AT DIFFERENT SCALES

(a) *Environmental conditions*

Satellite GOES-8 visible imagery, ground-based observations as well as forecasts made with the NCAR/PSU mesoscale model MM5 (Grell *et al.* 1995)* Version 3

* This paper, and other details of MM5, are available at http://www.mmm.ucar.edu/mm5/doc1.html

(4-km resolution on a domain centred on Homestead) have been used here to describe the environmental conditions on 14 June 2002. The day was characterized by high mean-sea-level pressure (1016 hPa or more) and light wind (less than 5 m s^{-1}) in the domain of interest. Surface winds were blowing from the north-east 1200–1500 UTC (Fig. 2(a)), before progressively veering 1500–1800 UTC. After 1800 UTC, winds were from the southwest, over the Oklahoma panhandle (Fig. 2(b)). A band of mid-level clouds was present over the Oklahoma and Texas panhandles at 1200 UTC. This band was advected south during the day, but still covered the south-western part of the domain of interest 1200–1900 UTC (the period during which were conducted the operations around Homestead) as shown in Fig. 2.

Associated with the high pressure, a weak subsidence was present all day, as evident in soundings. MM5 simulations in forecast mode, and observations, show that across the operational domain, whereas the temperature field was quite homogeneous the moisture had a mesoscale NE–SW oriented gradient (about 3 g kg^{-1} over ~200 km). Large soil-moisture contents were reported that day, the result of heavy precipitation during the two previous days. The observed atmospheric-moisture gradient was found to be coherent with the spatial distribution of precipitation, as more rain felt over the south-west and south of the area.

The first convective plumes (shallow ones, about 50–100 m deep) were observed at 1330 UTC, by the Wyoming Cloud Radar on-board the UWKA. The thermals grew gradually (in depth and in width) with time. At 1900 UTC, they reached a depth of 1000 m. They were more vigorous at the far eastern end of the flight track. The first few cumuli were observed at 1500 UTC on the western side of the domain. During the day, they gradually extended their coverage from west to east of the operation area. The top of the BL reached 1500 m above ground level (AGL*) in the early afternoon at 1900 UTC.

(b)   *Mesoscale variability*

Thirty-five soundings were launched during the day in a 200×200 km^2 zone around the Homestead profiling site (36.56°N, 100.61°W, cf. Fig. 1). Figure 3 shows soundings (black lines) launched between 1700 and 1730 UTC. At that time, both potential temperature, θ, and water-vapour mixing-ratio, r_v, are well mixed within the CBL, and the CBL top reaches a height of 1000–1500 m. At this scale (soundings are separated by several hundreds of kilometres), the range of variations of θ (r_v) reaches 2.5 K (5.5 g kg^{-1}) in the BL and 5 K (4 g kg^{-1}) in the free troposphere. The north-easternmost sounding (DDC in Fig. 1(a)) is the driest, with a mean water-vapour mixing-ratio of 5.5 g kg^{-1}, whereas the south-westernmost sounding (AMA) is the moistest, with a mean water-vapour mixing-ratio of 11 g kg^{-1}. This is consistent with the horizontal gradient found from the *in situ* aircraft data, and described later. In Fig. 3(b), fluctuations in the vertical profiles of water-vapour mixing-ratio at heights between 2.3 and 3.5 km, suggest a laminated structure in the free air well above the boundary layer.

In situ data from two aircraft, the UWKA and the P-3, confirm the existence of a moisture gradient in the PBL at this scale. Both aircraft flew at a height of around 350 m on successive legs, each approximately 100 km long and oriented WSW–ENE. The positions of the legs flown between 1630 and 1730 UTC are shown in Fig. 1(b). Figures 4(a) and 4(b) show the time series of r_v and the vertical velocity w measured on board the P-3 from 1100 to 1800 UTC. Similar trends were found in the UWKA data

---

* In the following all heights are AGL; the area is mostly flat at an average altitude of 850 m above mean sea-level.
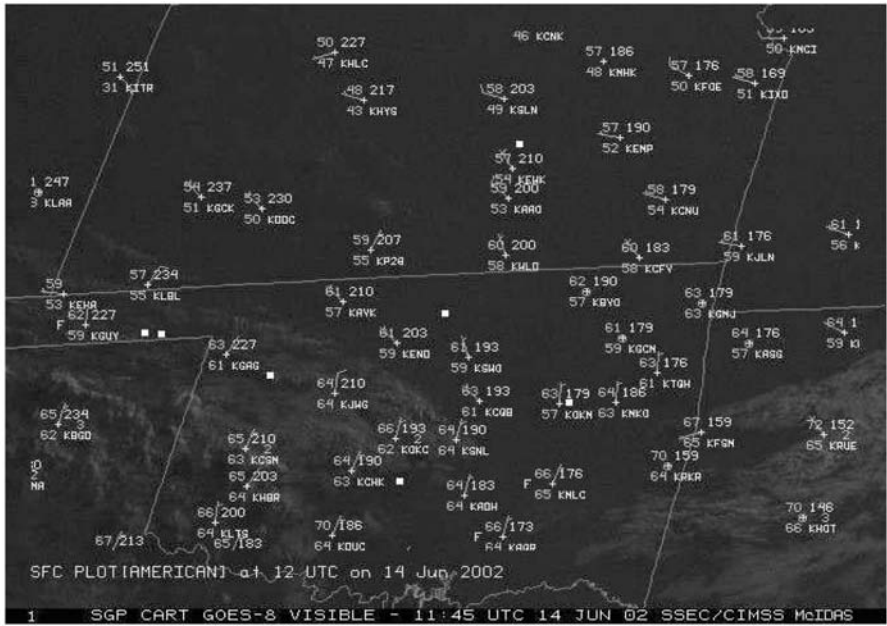
(a)
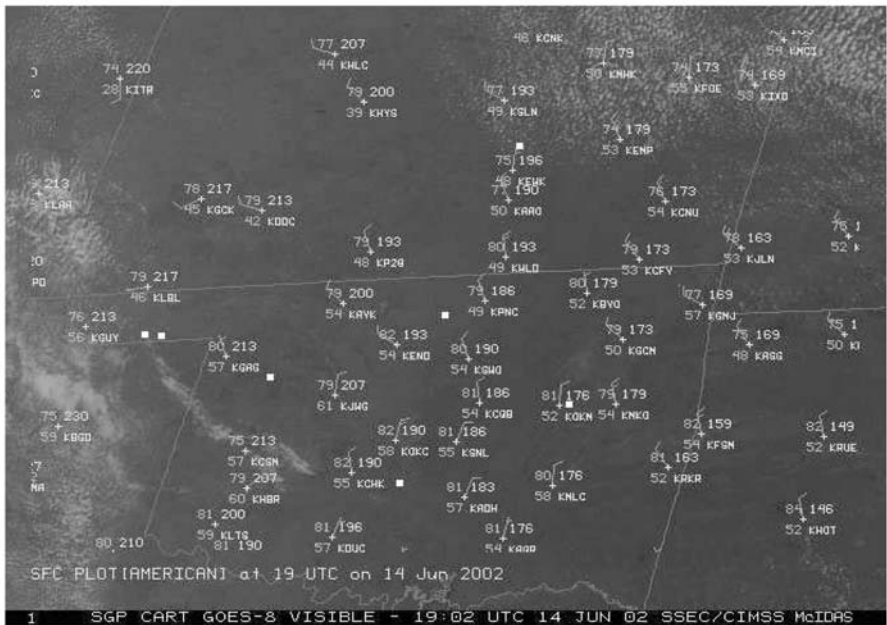
(b)

Figure 2. Satellite GOES-8 images at visible wavelength with superimposed surface observations, each showing, top-left surface air temperature (°F), bottom-left surface dew-point (°F), surface wind vectors (full- and half-barbs denote 10 m s^{-1} and 5 m s^{-1} respectively), top-right mean sea level atmospheric pressure (hPa and tenths with first two digits omitted) and bottom-right station identifiers: (a) 1200 UTC 14 June 2002 and (b) 1900 UTC 14 June 2002. Lines denote state borders within the United States.
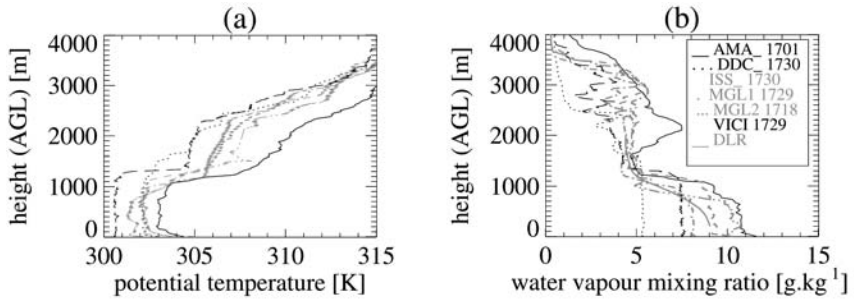
Figure 3.   Vertical profiles from soundings on 14 June 2002 around 1700 UTC: (a) potential temperature (K) and (b) water-vapour mixing-ratio (g kg^{-1}) (for which the light grey solid line denotes the mean DIAL lidar profile obtained from three segments centred over Homestead between 1700 and 1730 UTC). In both panels, other grey lines denote soundings launched in the sub-domain shown in Fig. 1(b).

(not shown). In Fig. 4(b), the successive flight legs show the existence of a moisture gradient. At 1200 UTC, the difference between the south-western end (moist) and the north-eastern end (dry) is around 2 g kg^{-1}; this difference increases throughout the day and reaches 3.5 g kg^{-1} at 1700 UTC. Such a gradient does not appear in vertical velocity (Fig. 4(a)) nor in potential-temperature data (not shown). Figures 4(c) and 4(d) show the decomposition of r_v into $r_v = \langle r_v \rangle + r_v'$, with $\langle r_v \rangle$ the 10 km running mean and r_v' the fluctuation about this mean for the leg beginning at 1715 UTC. It shows that both mesoscale (corresponding to hydrostatic phenomena with scale larger than 10 km) and submesoscale (corresponding to non-hydrostatic phenomena with scales smaller than 10 km) contribute to the observed variability in r_v. The airborne DLR DIAL (Ehret *et al.* 1999) also captures this mesoscale variability (not shown).

(c)   Submesoscale variability

Twenty-seven soundings were launched within a 40×10 km^2 restricted area (centred on Homestead). Figure 5(a) shows profiles of θ and Fig. 5(b) of r_v measured by the different soundings for this area around 1200 UTC. At this time, the profiles show the air to be stable to vertical displacements with a weak horizontal variability. The range of mixing-ratio fluctuations, of the order of 1 g kg^{-1} below 500 m, stands in contrast to the more uniform value above 1500 m even though laminated structures are present at higher altitudes. The soundings can be divided into two groups according to the mesoscale moisture-gradient as described previously. The eastward soundings (MCLASS and ISS) are characterized by drier air in the residual layer than the westward soundings (MGL1 and MGL2). The grey soundings of Fig. 3 correspond to the ones launched in this area at 1700 UTC (local midday). At this smaller scale, the sounding measurements of θ vary by less than 1 K in the BL and around 1.5 K in the free troposphere. The fluctuations of r_v among soundings are 2 g kg^{-1} in the BL and less than 0.5 g kg^{-1} in the free troposphere, underlying the relative homogeneity of the air masses above the BL in this area. These variations are in agreement with those found by Weckwerth *et al.* (1996). Note that the range of fluctuations in the free troposphere lies within the accuracy of radiosonde measurements (0.5 g kg^{-1}) reported by Wang *et al.* (2002), whereas the fluctuations in the BL are much larger than it, and so are significant. Note, too, that the water-vapour profile derived from three segments of DLR DIAL measurements (see section 5) is in the range of fluctuations inferred from radiosondes. Moreover, the fluctuations at the submesoscale increase during the day from 1 g kg^{-1} before 1500 UTC to 2 g kg^{-1} at 1730 UTC (also confirmed by *in situ* aircraft-data). It is somewhat artificial
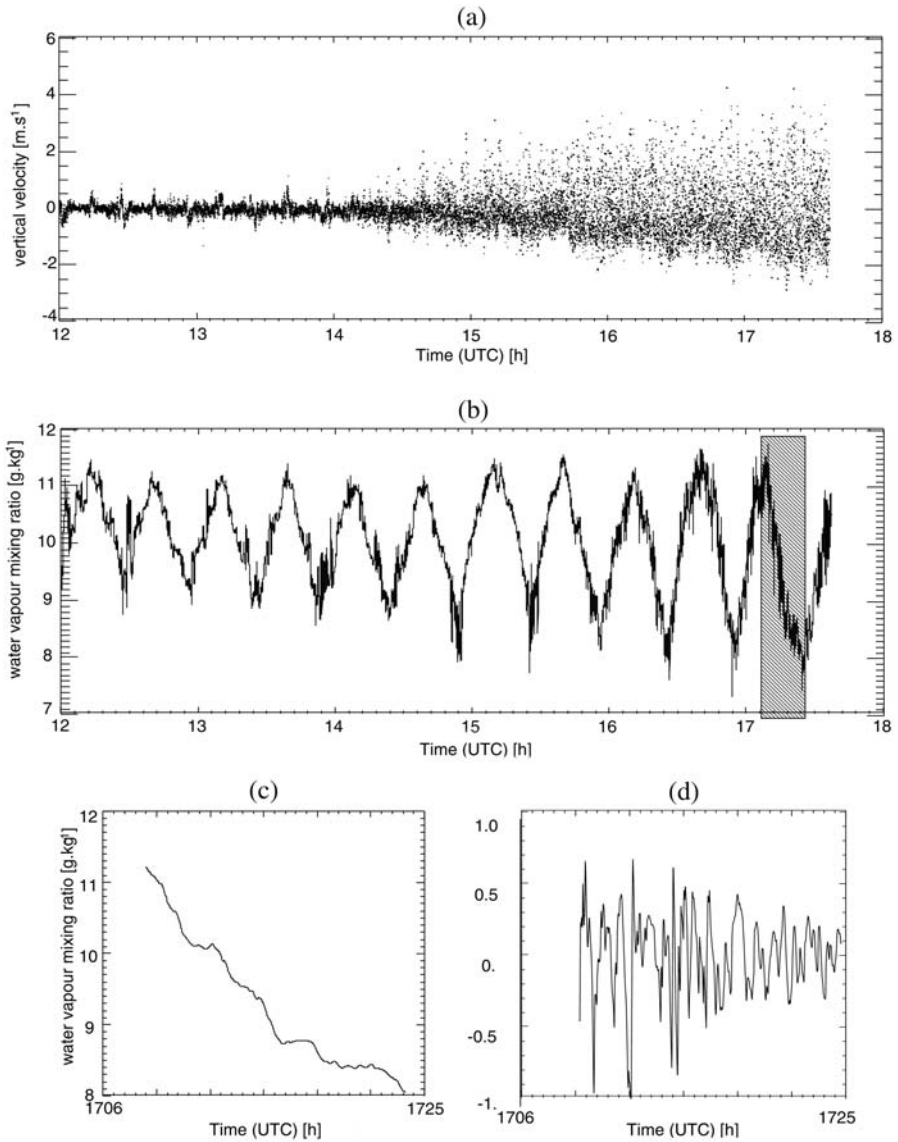
Figure 4. Time series derived *in situ* from the P-3 at 1 Hz frequency on 14 June 2002: (a) vertical velocity (m s^{-1}) 1200–1740 UTC; (b) water-vapour mixing-ratio (g kg^{-1}) 1200–1740 UTC; (c) water-vapour mixing-ratio (g kg^{-1}) on the mesoscale 1706–1725 UTC, and (d) variability of water-vapour mixing-ratio (g kg^{-1}) on the submesoscale 1706–1725 UTC.

to ascribe variability in soundings to one or the other scale since even in the restricted area, the signature of the mesoscale moisture gradient is also observed (as shown by the separation of 1200 UTC soundings into two groups). From the analysis of the previous subsection, a maximum fluctuation of 0.35 g kg^{-1} could result from this gradient for distances of 10 km.

No mesoscale variability can be found in the aircraft time-series of w but strong fluctuations exist at submesoscale (Fig. 4(a)). These fluctuations increase significantly after 1430 UTC both because of increasing turbulence and the aircraft's then flying
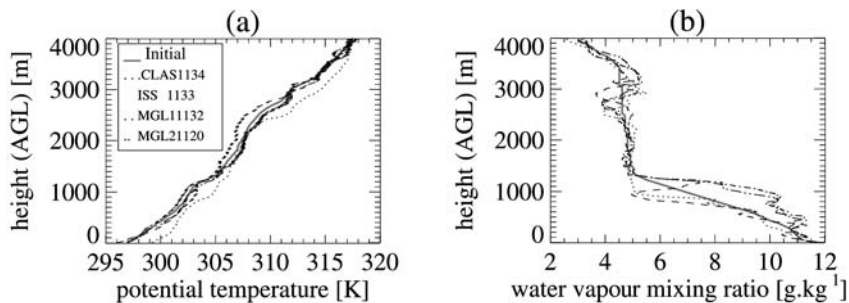
Figure 5.   Initial vertical profile (continuous grey line) used in the simulation, and soundings launched in the sub-domain (black) around 1200 UTC 14 June 2002, used to create the composite profiles: (a) potential temperature (K) and (b) water-vapour mixing-ratio (g kg^{-1}).

within the BL. In the following, we focus on results after 1500 UTC since, by then, the BL has clearly become convective (as indicated by the large fluctuations of the vertical velocity at small-scale). Note that this increase of small-scale fluctuations is also captured by the other *in situ* aircraft-data. Figure 4(d) shows the submesoscale contribution to the r_v variability of one leg. Fluctuations are significant and of the order of 1–1.5 g kg^{-1} (the accuracy of an aircraft measurement is around 0.3 g kg^{-1}). The airborne DLR DIAL also measures the small-scale variability as shown later, in section 5.

These data underline how various scales are involved in the observed modes of variability, probably associated with distinct processes. In the following section, we use an LES approach to focus on the submesoscale variability. The impact of atmospheric mesoscale variability on the submesoscale variability is analysed by distinguishing the impact of advection, surface fluxes and initial conditions.

3.   LARGE-EDDY SIMULATION (LES) CONFIGURATION

(a)   *Model and domain*

The model used in this study is the LES version of the non-hydrostatic model Meso-NH, the dynamical part of which was presented by Lafore *et al.* (1998). The 3-D turbulence scheme is based on that proposed by Redelsperger and Sommeria (1982; 1986) and was discussed in detail by Cuxart *et al.* (2000). It is based on a prognostic equation for subgrid kinetic energy and it incorporates the effect of thermal stratification on subgrid fluxes through variable Prandtl and Schmidt numbers.

A 10 km × 10 km × 5 km domain is defined, centred over Homestead (see Fig. 1(b)). The horizontal resolution is 100 m. A vertical stretched grid of 60 levels is used with resolution finer than 50 m in the BL and up to 2000 m, and coarser higher up (reaching 250 m at the top of the model). The lateral conditions are cyclic. The simulation starts from horizontally homogeneous conditions, except for a random θ perturbation of 0.1 K applied to each grid point of the lowest level. Large-scale advections of heat and moisture have been taken into account, since data indicate that they were not negligible during the observing period. This point is discussed later in subsection 4(c). A nudging towards the observed wind has been applied to the mean wind, so as to ensure that the simulated profile is realistic. Note that this nudging has almost no impact on our results here since the wind is light (less than 5 m s^{-1}). Sensitivity tests on domain size (test with a 15 km × 15 km × 5 km domain) and horizontal and vertical resolution all gave similar results, including the characteristics of
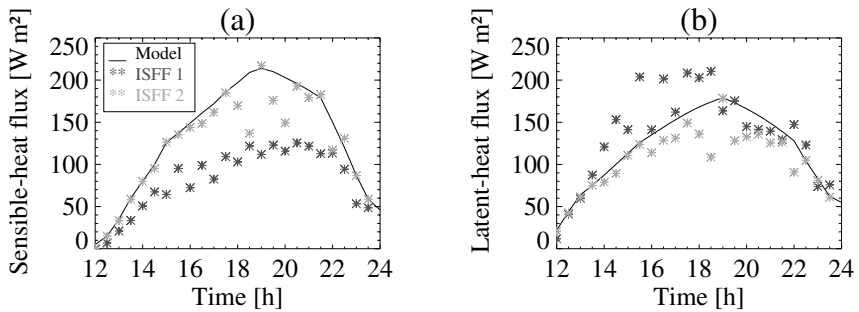
Figure 6. Fluxes (stars) measured between 1200 UTC and 2400 UTC on 14 June 2002 by the two flux stations ISFF-1 (black) and ISFF-2 (grey) closest to Homestead: (a) sensible heat and (b) latent heat. The black lines show the surface fluxes prescribed in the reference LES experiment.

horizontal structures, so that we are confident that the results we present do not depend on the choices we made.

(b) Initial conditions and forcing

The goal of the simulation is to reproduce the diurnal development of the BL from early morning to early afternoon. Consequently, the model is run from 0700 to 1400 LT (1200 to 1900 UTC). Beginning the simulation at 1200 UTC allows a more than sufficient spin-up time before the significant deepening of the BL (as observed from aircraft at 1500 UTC, for example).

Observations are dedicated to two separate goals. Specific data are used to initialize the simulation and to prescribe the surface conditions, whereas other independent observations are used to evaluate the simulation. Soundings in the morning (Fig. 5) and surface-flux measurements (Fig. 6) are used to prescribe initial vertical profiles and time-varying surface fluxes, respectively (see the appendix for the values). Other soundings, aircraft *in situ* data and lidar data are used to check the quality of the simulation, with an emphasis on the water-vapour field.

The initial vertical profiles for the reference (REF) simulation are obtained from a composite of the soundings launched around 1130 UTC in the operational area (Fig. 5). Following Brown *et al.* (2002), time-varying horizontally homogeneous surface-fluxes derived from observations are prescribed. The advantage of such an approach is that it is simple and ensures that the energy input from the surface remains close to observations. Note that the domain is 10 km wide, so that neglecting sub-domain circulations induced by surface heterogeneities appears to be a reasonable assumption (Hechtel *et al.* 1990; Avissar and Schmidt 1998; Letzel and Raasch 2003). The prescribed surface fluxes are derived from the measurements made at the Integrated Surface Flux Facility (ISFF), located near Homestead, shown in Fig. 6. (Local spikes caused by the presence of scattered clouds have been removed). The measured surface-flux differences between ISFF-1 and 2, larger latent-heat flux and smaller sensible-heat flux at the southern station, are consistent with more precipitation having fallen in the south. In the REF simulation, we used interpolation of the measurements by the ISFF-2 (indicated by a black line in Fig. 6) because they appear to be more representative of the observed BL evolution over the area.

As discussed in section 2, important advection of moisture occurs at scales greater than 10 km. Here, this forcing (hereafter referred to as large-scale advection) is
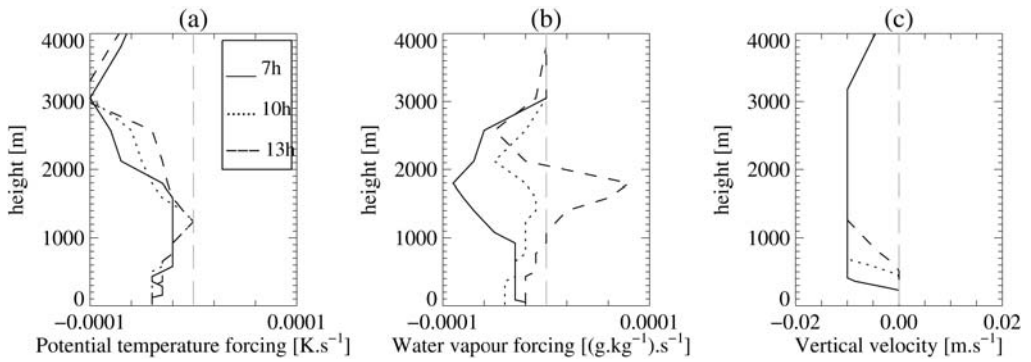
Figure 7.   Figure 7. Vertical profiles of large-scale advection at 1200 UTC (solid), 1500 UTC (dotted) and 1800 UTC (dashed) prescribed in the simulation: (a) horizontal advection of potential temperature (K s^{-1}); (b) horizontal advection of water-vapour mixing-ratio (g kg^{-1}s^{-1}), and (c) vertical velocity (m s^{-1}).

prescribed in order to represent the effects which cannot be allowed for by using cyclic lateral boundary conditions (values of forcing are given in the appendix). Even though the surface fluxes are mainly responsible for the diurnal cycle of the BL, large-scale advection was found necessary to get a more realistic simulation (see section 4). In practice, however, it is delicate to retrieve such large-scale advection from sparse isolated observations alone (Mace and Ackerman 1996). Consequently, it has been deduced from numerical simulations performed with the MM5 model during IHOP_2002 (Couvreux *et al.* 2002). We did so because MM5 results were very consistent with the sounding data for this day, and at the same time provided a complete time-varying data-set. Large-scale forcing is imposed via horizontal advection (of θ and r_v) and subsidence (cf. Fig. 7). The advection of θ (Fig. 7(a)) is responsible for an overall cooling and the advection of moisture (Fig. 7(b)) for a general drying, except for some moistening between 1200 m and 2000 m at 1800 UTC. The moisture advection is significant only below 3000 m. Calculations from soundings gave similar values for temperature and humidity horizontal advection. As previously noted, a weak subsidence is observed during the whole simulation period. The prescribed value, deduced from MM5 results (Fig. 7(c)) is -0.01 m s^{-1} above the BL.

(c)   *Sensitivity analyses*

Sensitivity experiments have been performed in order to assess the impact of the initial profiles, surface heat-fluxes and the large-scale advection. They also aimed at quantifying the impact of mesoscale variability (through impact of surface fluxes, advection and initial profiles) on the mean properties of PBL. A first sensitivity experiment was conducted using surface-flux measurements from the ISFF-1 instead of ISFF-2. The experiment is referred to as LOWBo (the Bowen ratio (Bo) was on the order of 1.1 and 0.5 for ISFF-2 and ISFF-1, respectively). The impact of the large-scale advection of heat and moisture was treated in the NOADV experiment. Finally, two experiments (DRY and MOIST) were designed to analyse the impact of the initial sounding: the DRY experiment used a drier sounding than the initial composite sounding (namely, the ISS sounding at 1130 UTC) whereas the MOIST experiment used a moister one (namely MGL2 at 1120 UTC). Results from these sensitivity analyses are discussed in section 4.
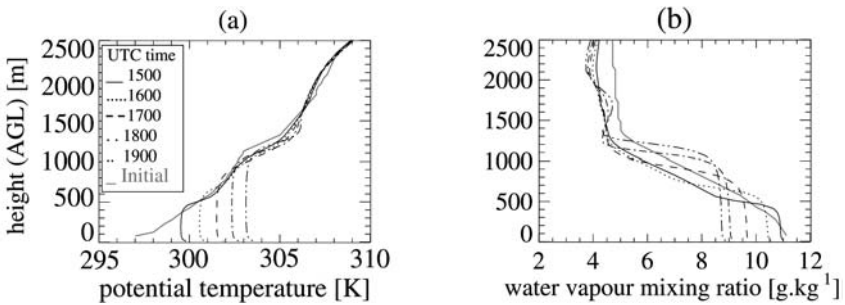
Figure 8. Evolution of simulated vertical profiles, hourly between 1500 UTC and 1900 UTC 14 June 2002: (a) potential temperature (K) and (b) water-vapour mixing-ratio (g kg^{-1}). In each panel, the grey line shows the initial profile.

4. AVERAGE PROPERTIES OF THE SIMULATED CBL AND SENSITIVITY ANALYSES

(a) Average properties of the reference simulation

Figures 8(a) and 8(b) show the evolution of the simulated mean profiles of θ and r_v. From 1500 UTC to the end of the simulation, the air in the CBL is well mixed: θ is constant with height, except for a superadiabatic layer close to the surface. As is often observed in the morning in fair weather over land, the BL rapidly warms and deepens, in response to the increase of surface sensible-heat flux. The temperature gradient across the CBL top increases until 1700 UTC and then decreases. This evolution results from the effects of surface heating, subsidence, entrainment, stratification in the free troposphere and BL growth-rate (e.g., Tennekes 1973). At any one time, the water-vapour mixing-ratio is also almost constant with height but the BL progressively dries, with a mean value of r_v decreasing from 11 g kg^{-1} at 1500 UTC down to 8.8 g kg^{-1} at 1900 UTC. Such a drying is consistent with the significant deepening of the BL as frequently observed (Mahrt 1991), although not systematically over this region (Zhu and Albrecht 2002). The strength of the water-vapour mixing-ratio jump at the CBL top increases in the morning, reaching about 4 g kg^{-1} at 1800 UTC. It is explained mainly by the growth of the BL into drier layers aloft. The moister layer observed in the free air above the CBL top, at about 1700 m and 1800 UTC and 1900 UTC, results from the large-scale moisture advection which is significantly positive at heights around 2000 m at 1800 UTC (cf. Fig. 7(b)).

The ratio of the sensible-heat flux at the top of the mixed layer to that at the ground is -0.2, indicating conditions close to a purely convective case (e.g., Deardorff 1972; Tennekes 1973; Schmidt and Schumann 1989). The mean buoyancy flux-ratio is around -0.11, showing the importance of water vapour in the buoyancy flux (the mean latent-heat flux-ratio is 1.5). This value of the mean buoyancy-flux is close to those obtained by Fedorovich *et al.* (2004) with LES for purely convective regimes of the BL, and consistent with other previous LES studies (Cuxart *et al.* (2000) among others).

The simulated mean profiles of θ and r_v have been systematically evaluated against available soundings and water-vapour DIAL data. As an example, Fig. 9 shows the data obtained at 1800 UTC. Here, the LES profiles correspond to domain-mean values whereas the soundings correspond to local measurements. Overall, the simulated profiles lie within the range of observations, in the BL as well as above. Note that,
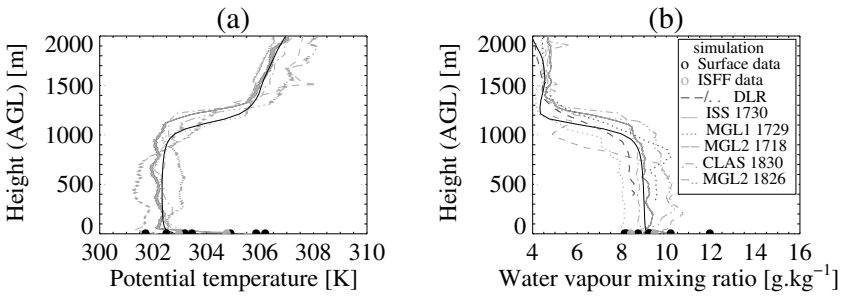
Figure 9. Vertical profiles around 1800 UTC 14 June 2002 observed by radiosonde (grey) and simulated (black): (a) potential temperature (K) and (b) water-vapour mixing-ratio (with mean DIAL lidar profiles (bold dark grey lines) for 1732–1733 UTC and 1733–1734 UTC).

based on 10 000 profiles in the simulation, the standard deviation of θ is 0.1 K and of r_v 0.35 g kg^{-1}; the ranges of the fluctuations are 1 K and 3 g kg^{-1} respectively. This degree of variability is comparable to that observed on 14 June 2002, and is broadly consistent with values reported elsewhere (Weckwerth *et al.* 1996). The strength of the jump in temperature and humidity at the BL top is well predicted: an increase, at a height of about 1100 m, of about 3 K in θ and a decrease of 3 g kg^{-1} in r_v.

Figure 10 presents the evolution of the height (z_i) of the top of BL, the mean potential temperature (θ^m) and water-vapour mixing-ratio (r_v^m) in the CBL derived from the REF simulation between 1500 and 1900 UTC. In the simulation, the CBL height is derived using the method described by Wulfmeyer (1999), based on the determination of the height in the profile at which the absolute value of the vertical moisture-gradient— ($\partial r_v / \partial z$)—is a maximum. The growth of the BL is significant, with z_i increasing from 500 m at 1500 UTC to 1200 m at 1900 UTC. This significant deepening of the BL typifies the daytime deepening of the CBL over land, as compared with its steadier state over the sea. The simulated variations of z_i, θ^m and r_v^m with time are consistent with sounding measurements (stars in Fig. 10), with the exception of the simulated r_v around 1530 UTC which appears to be overestimated with respect to the observations (possibly the result of an underestimation of large-scale advective drying at that time). The simulated mixed-layer values of θ^m and r_v lie in the middle of the range of variability given by the soundings (around 1 K and 2 g kg^{-1} respectively).

Overall, this simulation provides a realistic picture of the mean characteristics of a CBL in this growing phase.

(b) Sensitivity to initial conditions and forcing

Figure 10 allows z_i, θ^m and r_v^m derived from the sensitivity experiment LOWBo, NOADV, DRY and MOIST to be compared to their REF counterpart. When comparing LOWBo with REF, we find that: z_i is lower in LOWBo than in REF with a difference reaching 300 m at 1800 UTC; consistent with a lower surface sensible flux, θ^m is less by 1 to 1.5 K (the difference increases with time), and r_v^m is greater by 0.7 to 1.3 g kg^{-1}. Sounding data show that the LOWBo simulation underestimates z_i and θ^m (because of lower values of the sensible-heat flux) and overestimates r_v^m (a result of the higher surface-moisture flux being mixed through a shallower BL).

The comparison of REF with NOADV indicates that: z_i is lower in REF, with a difference increasing with time up to 300 m, the prescribed subsidence explaining
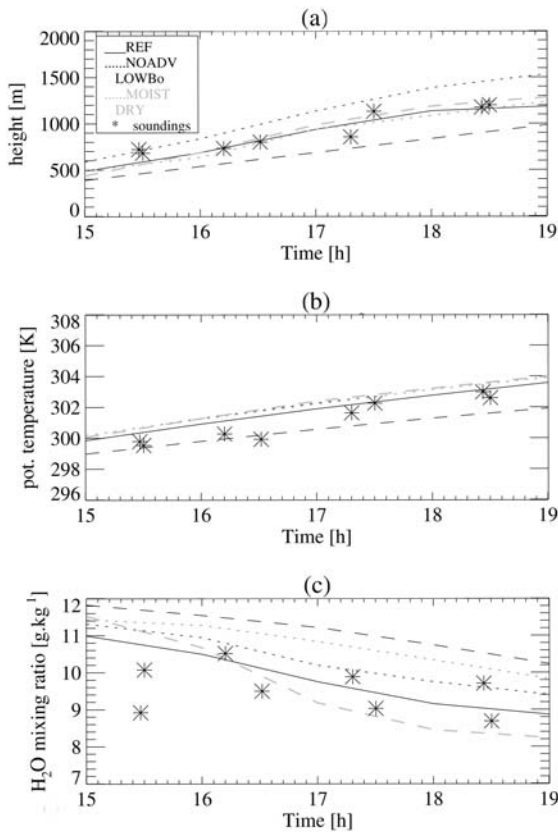
Figure 10. Time series for the reference simulation (continuous line) and simulations NOADV (dashed), LOWBO (dotted), MOIST (grey dotted) and DRY (grey dashed): (a) height of boundary-layer top (m); (b) potential temperature in the boundary layer (K) and (c) water-vapour mixing-ratio in the boundary layer (g kg^{-1}). Stars denote values obtained from soundings.

most of the difference; θ^m is 0.3 to 0.5 K lower, resulting from opposite effects of subsidence bringing warmer air from above the BL and horizontal advection of cooler air; r_v^m is 0.5 g kg^{-1} drier, combining effects of the entrainment of subsiding dry air and the advection of dry air. Thus, the large-scale advection induces important modifications θ^m and r_v^m, although smaller than the ones induced by changing surface-fluxes. Better agreement with observations is found for BL z_i, θ and r_v obtained from the REF than from the NOADV simulation. Even though the initial temperature profiles and surface fluxes prescribed in REF, DRY and MOIST are identical, z_i is slightly higher for DRY and θ^m slightly warmer, whereas θ_v^m is slightly cooler because of a drier r_v^m. By contrast, differences in r_v^m between DRY and REF simulations are significant and increase during the day reaching -0.6 g kg^{-1}; similarly, those between MOIST and REF reach $+1$ g kg^{-1}. The variances also differ: until 1700 UTC, DRY has larger values at z_i than MOIST, chiefly because of a stronger moisture gradient at the BL top. In turn, this stronger gradient arises partly because the top is slightly higher but mostly because the initial profile was drier as a result of the previous day's deepening of the BL. Potential temperature variance is also larger for DRY due to a slightly larger z_i and a stronger gradient at the BL top (not shown).

5.   VARIABILITY OF THERMODYNAMICAL VARIABLES IN THE CBL

(*a*)   *Horizontal and vertical variability*

During the simulation, horizontal structures evolve in the BL. After two hours of simulation, for example, rolls with horizontal axes oriented more or less along the wind, are present across the domain. This is consistent with the moderate value of the ratio of the CBL depth to the Monin–Obukhov length, $-z_i/L_{MO}$, i.e. about 25 (e.g., Deardoff 1972). Later on, greater instability causes the rolls to be replaced by cellular convection (from 1500 to 1900 UTC, $-z_i/L_{MO}$ is much greater than 45). Figure 11 presents horizontal cross-sections of the simulated r_v, θ and vertical velocity (w) at different heights corresponding to $z/z_i = 1$, 0.8, 0.5, 0.3 at 1800 UTC. For clarity, only the north-western quarter of the domain is shown. At $z/z_i = 0.3$, only a few thermals are visible, but they are strong and there is a strong correlation between perturbations in θ and w. This illustrates the role of temperature anomalies in the buoyancy at this level. At $z/z_i = 0.5$ and 0.8, the θ field is more homogeneous as a result of strong mixing and of a decreasing positive buoyancy. By contrast, inertia still keeps w positive (the maximum of w perturbations occurs at $0.4\,z_i$). At $z/z_i = 1$, potential temperature fluctuations are organized into large structures, with wide zones of negative anomalies and narrow zones of positive anomalies. The former correspond to thermals, which cease rising at the BL top and therefore spread out. The latter correspond to the intrusion of warmer air into the mixed layer originating from higher levels. This contrasts with the classic view of very shallow and rapid updraughts and large slow descending zones. Only very restricted ascending zones persist in the core of thermals, corresponding to the overshooting part. At $z = z_i$, the correlation between fluctuations in r_v and θ is strongly negative ($r \leqslant -0.9$) as commonly observed (Wyngaard *et al.* 1978; Berg and Stull 2004). At all levels, r_v fluctuations tend to occur in the form of larger structures (with spatial scale around 1 to $2\,z_i$). Moreover starting from the top row of panels in Fig. 11, structures are easily followed from one horizontal section to another, confirming the strong correlation coefficients found between different levels. Dry tongues originating from the entrainment layer seem to impose a characteristic length-scale to CBL r_v fluctuations. They impact the PBL at least down to $0.3\,z_i$ where dry pockets are still present (min of $r_v \sim 5.7$ g kg^{-1}). They are also obvious in vertical cross-sections (cf. Fig. 13 for instance). To quantify this, integral length-scales (Li), following Lenschow and Stankov (1986), were calculated*. They indicate systematically larger Li for r_v (0.3–$0.4\,z_i$) than for θ (0.1–$0.3\,z_i$), θ_v (0.1–$0.25\,z_i$) and w (0.07–$0.2\,z_i$) in agreement with De Roode *et al.* (2004). For example, at 1800 UTC (Fig. 12), Li for r_v decreases from $0.4\,z_i$ near the surface to $0.25\,z_i$ at the top of the mixed layer. The decrease of Li with height is consistent with dry tongues penetrating the CBL and becoming less and less numerous towards the lowest levels. For w, Li ranges between $0.1\,z_i$ and $0.2\,z_i$ with a maximum at $0.4\,z_i$ where the updraughts are stronger. For θ, Li grows from $0.1\,z_i$ at the surface to $\sim 0.25\,z_i$ at the top of the mixed layer; this is explained by the presence of fewer thermals as height increases. In the lower part of CBL, the length-scale for θ_v is similar to that for θ but not for w. In the upper part of CBL however, the larger-scale fluctuations of θ and r_v partly compensate, leading to smaller θ_v length-scale. This is in partial agreement with De Roode *et al.* (2004) since their study (based on academic LES simulations) indicates such compensation but through the whole BL. The different types of BL could explain this difference: we focus on a growing CBL over land (strong diurnal variation of surface fluxes) whereas the BL

---

* Note that computation using a geometric scale proposed by Lohou *et al.* (2000) leads to the same conclusion.
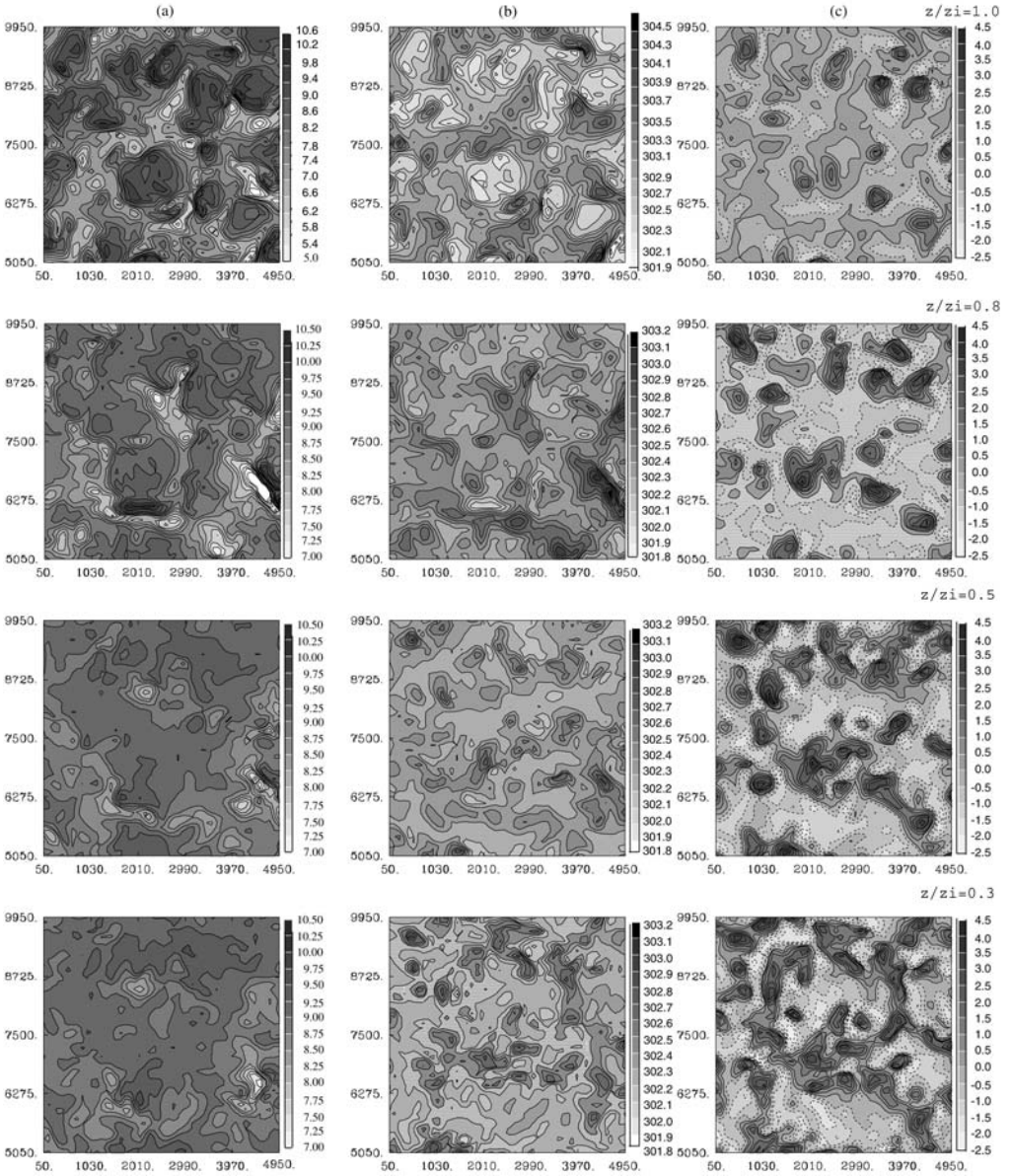
Figure 11. Horizontal cross-sections of the north-western quarter of the domain at $z/z_i = 1.0$, 0.8, 0.5 and 0.3 of simulated values at 1800 UTC on 14 June 2002: (a) water-vapour mixing-ratio (g kg^{-1}); (b) potential temperature (K) and (c) vertical velocity (m s^{-1}).

of De Roode *et al.* (2004) is more representative of quasi-stationary oceanic conditions (Bowen ratio Bo $\sim$0.15).

A vertical cross-section of water-vapour mixing-ratio extracted from the REF simulation along a southwest-northeast oriented axis at 1700 UTC is shown in Fig. 13(a). Fluctuations of the BL height (defined as in section 4) are on the order of 200–300 m,
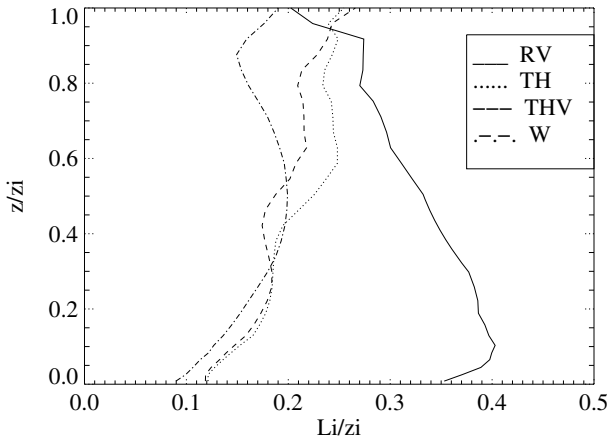
Figure 12.   Vertical profiles of integral (non-dimensional) length-scale at 1800 UTC 14 June 2002: potential temperature (dotted lines); water-vapour mixing-ratio (solid); virtual potential temperature (dashed) and vertical velocity (dash-dot).

consistent with DIAL observations (Fig. 13(b)). Two tongues of relatively drier (negative perturbation -1 g kg^{-1} to -2 g kg^{-1}) and sinking air are found. The south-western one extends from the BL top to the ground bringing very dry air close to the surface. Such phenomena have already been proposed by Mahrt (1991) to explain the existence of dry pockets observed by aircraft in the lower part of BL. Our simulated structures are consistent with those obtained by Sullivan *et al.* (1998) under similar moderate inversion strength conditions (in the present case the θ_v jump at PBL top is around 3 K). Their simulations exhibited narrow zones of warm air dipping down into the BL on the edges of thermals. Indeed, they show that, depending on the inversion strength, the shape of the subsiding intrusions is different (sharper for strong temperature-inversion). Here, since the inversion is also characterized by a strong variation in r_v, this descending air is also very dry. The vertical-velocity field (overplotted on Fig. 13(a)) illustrates the complex circulations taking place in the BL. Note how one positive r_v perturbation zone can be associated with several updraughts. Below 500 m ($\sim$0.67 z_i), dry tongues have essentially negative buoyancy, relative to their moister environment, and therefore subside. The dryness actively contributes to this negative buoyancy, as assessed by different θ and θ_v. However, neglecting the contribution of water vapour to the buoyancy in the simulation does not suppress these dry tongues: the potential temperature adjusts to the presence of water vapour to maintain the boundary layer's overall equilibrium balance. Figure 13(b) presents a vertical cross-section of water-vapour mixing-ratio measured by the DLR DIAL between 1717 and 1718 UTC. For this 9 km long segment, the BL height also shows a strong variability. Several dry tongues (with perturbations of -1 to -2.5 g kg^{-1}) reaching 0.4 z_i are present, even drier than simulated. The simulated moisture field is consistent with these observations. Both cross-sections are representative of observations and simulations, even though dry tongues are not always as dry nor do they often reach the ground. In Fig. 13(c), an example of r_v time series measured by the UWKA is shown (8 km long leg). It shows two dry zones whose dryness is representative of that commonly observed and simulated that day.

The lifetime of these dry tongues is around 20–30 minutes in the LES, indicating that they might impact on non-local transport in the CBL. To characterize these dry
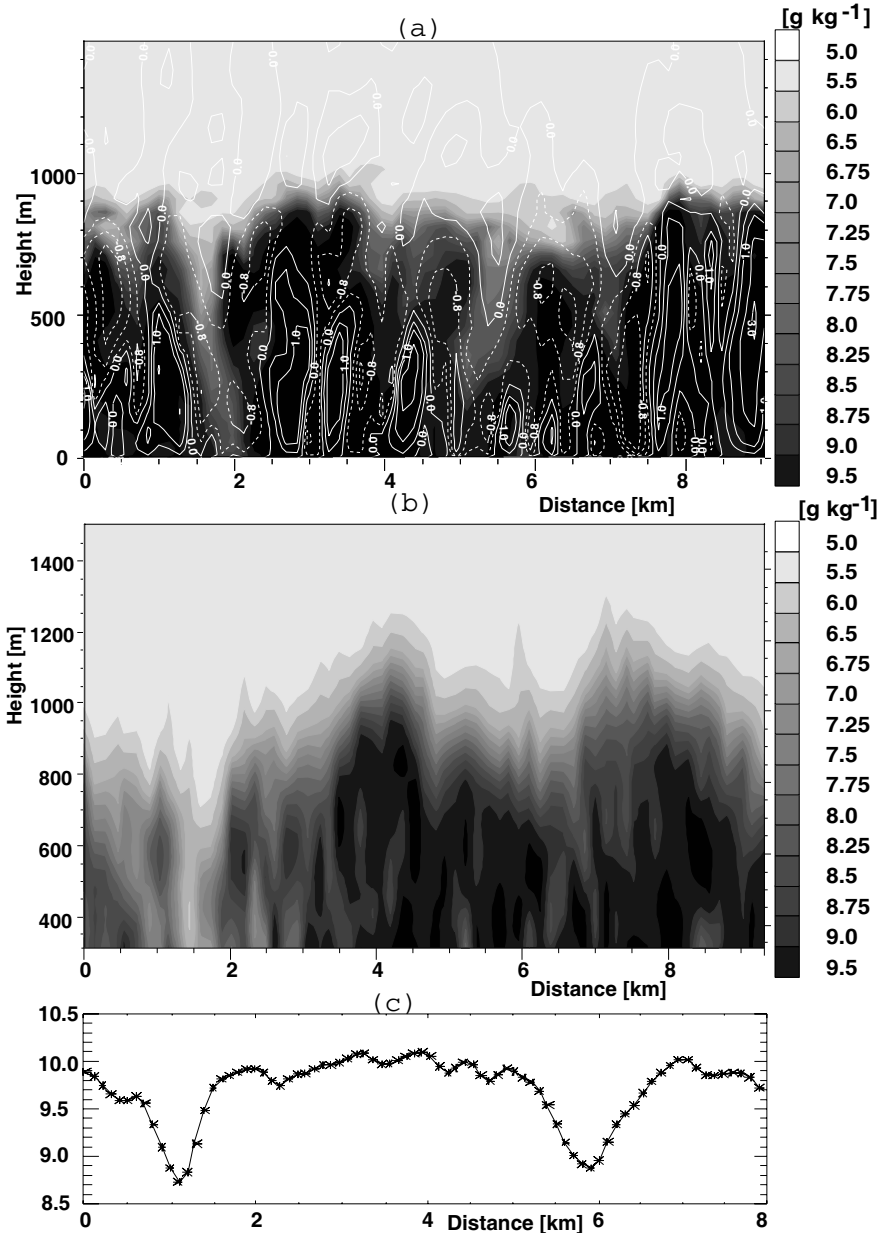
Figure 13.   Cross-sections of water-vapour mixing-ratio (g kg^{-1}): (a) vertical section simulated by the model for 1700 UTC (superimposed isotachs of vertical velocity are solid for ascent (0, 0.5, 1, 2, 3, 4 m s^{-1}) and dashed for descent (-0.4, -0.8, -1.2, -1.6 m s^{-1})); (b) vertical section observed by the airborne DLR-DIAL around 1715 UTC, and (c) linear section at 350 m from *in situ* UWKA measurements around 1700 UTC.

tongues, the criterion of r_v negative perturbation larger than the standard deviation at 0.8 z_i was retained in order to have a consistent criterion throughout the whole CBL. Using this criterion, the horizontal area occupied by dry tongues is greatest at z_i, where dry air occupies around 30% of the horizontal area, and decreases downwards towards the surface which only a few tongues reach (and occupy only a few per cent). In the lower part of the CBL, the area occupied seems to respond to the dynamic of entrainment of dry air since after 1800 UTC, when the BL grows more slowly, the area occupied by these dry tongues decreases. The number of dry tongues varies with height and time: there are more events close to z_i (around 100 per 100 km^2) than close to the surface (less than 10 per 100 km^2) and more events when the growth of the BL is greatest. At middle levels of the CBL, these tongues have typical diameters of a few hundreds of metres.

(b) *Probability distribution functions of thermodynamic variables*

We now focus on the probability distribution functions (PDFs) of θ, r_v, and w deduced from the simulation and from the observations. PDFs provide useful information, concerning the range of variations and the degree of asymmetry of the field under scrutiny. To validate the distribution of simulated values of w, θ and r_v, we use *in situ* data from two aircraft (P-3 and UWKA) obtained at ∼350 m (corresponding to ∼0.4 z_i at 1700 UTC). We use the 1 Hz data since the resulting horizontal resolution is close to that of the simulation, 90 m for UWKA and 140 m for P-3 (given average aircraft ground-speeds of 90 m s^{-1} and 140 m s^{-1} for the UWKA and the P-3, respectively). Fluctuations on scales larger than those simulated are estimated with a 10 km running mean and are subtracted from the time series. The coherence of spatial and temporal scales is fundamental here if comparisons with simulations are to be meaningful. Simulated and observed (minimum and maximum) distributions of w, θ and r_v, in the middle of the BL (at the flight altitude of the aircraft) have been compared. As an example, Fig. 14 shows observed and simulated PDFs for 1700 UTC on 14 June 2002. The P-3 and UWKA data from four consecutive legs flown between 1630 and 1730 UTC around Homestead (legs are about 80 km long) have been processed to infer an 'envelope of PDFs'. Figure 14 shows that, for all three variables, the simulated distribution is bounded by the minimum and maximum distributions derived from the aircraft *in situ* data. The positively skewed distribution of the vertical velocity (the skewness S is 0.8 for the LES, and varies from 0.7 to 1 for aircraft data) reflects the existence of few but strong updraughts and numerous but weak downdraughts as shown in Fig. 11. This is typical of a CBL heated from below (see, among others, Lemone (1990) and Moeng and Sullivan (1994)). The potential temperature has a quasi-symmetric distribution slightly positively skewed (S is 0.4 for the LES and varies from 0.4 to 0.9 for aircraft data). The water-vapour mixing-ratio, by contrast, is characterized by a negatively skewed distribution (it is however larger in LES with $S = -1.0$ than in aircraft data for which S varies from -0.2 to -0.8). Apart from numerical effects, this difference could be caused by the lack of horizontal variability in surface heat fluxes and initial profiles, as imposed by the LES configuration. However, the negative skewness of the observed and simulated r_v distributions reflects the presence of dry tongues originating from the entrainment layer (Fig. 13). The latter distribution is very different from that for vertical velocity, indicating that thermals alone cannot account for the observed distribution of water-vapour mixing-ratio. This may depend in various ways on the strength of the gradient of r_v and θ_v at the BL top. For smaller r_v gradients, the perturbation (negative anomaly) of air coming from above the BL can be of the same order as perturbation due to thermals (positive anomaly). Such a skewed distribution in the middle of the BL has already been observed over land by Crum and Stull (1987) and Weckwerth *et al* (1996).
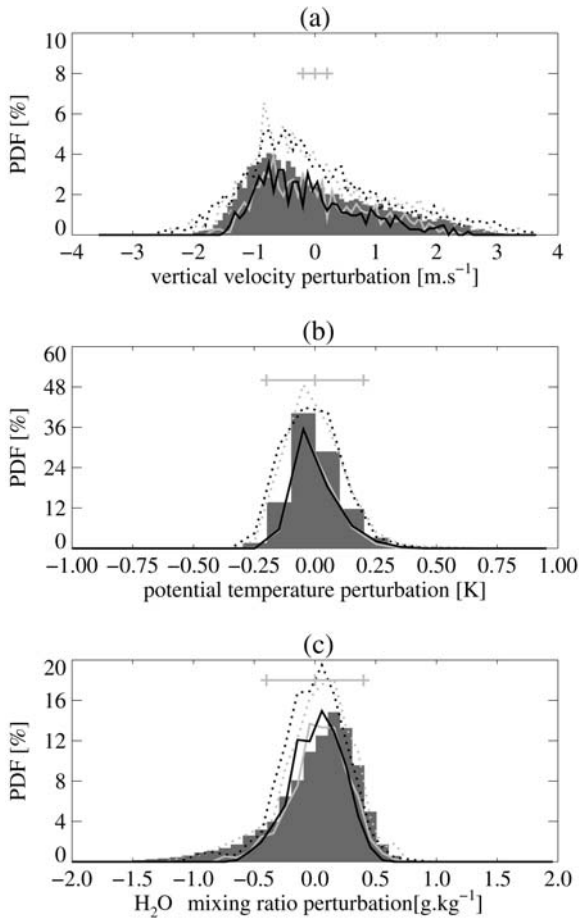
Figure 14. Probability density functions (PDFs) (%) at 350 m above local ground level around Homestead at about 1700 UTC 14 June 2002, derived from the simulation (shaded) and from observations (dotted lines denote the maxima, and continuous lines the minima, of PDFs derived from *in situ* measurements made from the UWKA (grey) and P-3 (black) on four flight-legs between 1630 and 1730 UTC): (a) vertical velocity; (b) potential temperature, and (c) water-vapour mixing ratio. Horizontal grey bars denote estimated errors of the *in situ* aircraft observations.

Figure 15 presents simulated water-vapour mixing-ratio PDFs at three different heights ($0.3\ z_i$, $0.7\ z_i$ and $1.0\ z_i$) at 1800 UTC. Because of the dry intrusions from the entrainment zone, the skewness of the distribution decreases with increasing altitude, ranging from -0.8 at $0.1\ z_i$ to -1.2 at $0.8\ z_i$. Above $0.8\ z_i$, the distribution is less skewed and becomes very flat because of the wide range of variations in a region where numerous intrusions and thermals coexist. At $z = 1.1\ z_i$, the distribution becomes positively skewed ($S = 2.3$) as a few thermals overshoot and introduce moist air into a relatively dry environment. Here, the presence of cumulus clouds (very few) does not modify the skewness. However, in other situations, their presence can favour positive skewness, as may be inferred from Fig. 2(d) of Larson *et al.* (2001). This sharp variation of moisture distribution with height seems typical of the CBL over land as assessed by analysis of aircraft *in situ* measurements from other IHOP_2002 days (not shown). Crum and Stull (1987) and Weckwerth (1996) reported similar evolution from observations.
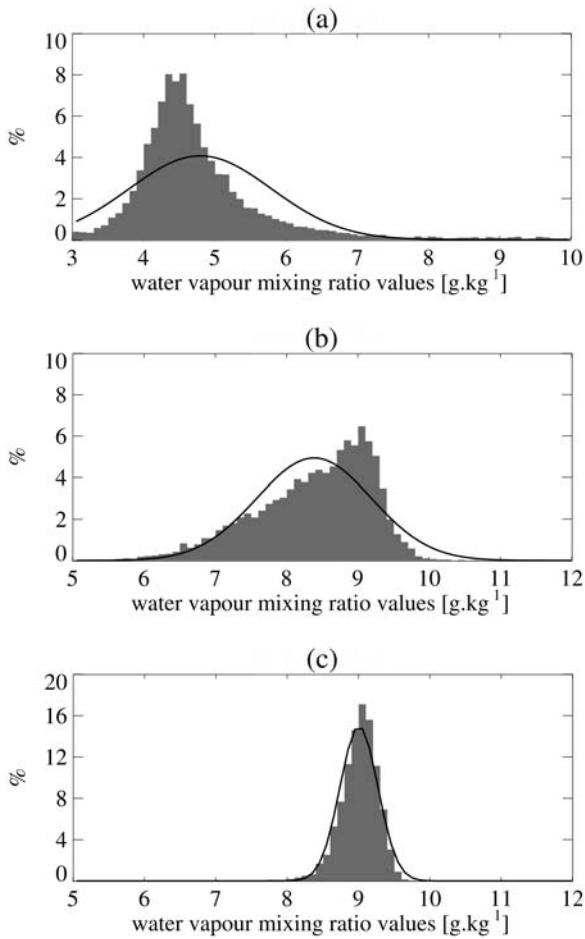
Figure 15.   Probability density functions (PDFs) (%) at about 1800 UTC 14 June 2002 of simulated water-vapour mixing-ratio at different heights and the equivalent Gaussian (i.e. normal) distribution with the same integral (black line) with a standard deviation σ: (a) $z/z_i = 1.0$, $\sigma = 1.3$; (b) $z/z_i = 0.7$, $\sigma = 0.44$ and (c) $z/z_i = 0.3$, $\sigma = 0.27$.

(c)   *Variance profiles*

In the LES simulation, the maximum of variance of both horizontal wind components, u and v, is found near the ground with a weaker peak at the top of the CBL. The maximum of the variance of vertical velocity w is located around 0.4 z_i. The variance of potential temperature θ has a relative maximum close to the surface and an absolute maximum around z_i as already presented in many previous studies (Mason (1989) and Cuxart *et al.* (2000) among others). For water vapour, the variance $r_v'^2$ is a key parameter in many cloud parametrizations (e.g., Bechtold *et al.* 1995; Price 2001). Moreover, from an observational point of view, it is also potentially useful since there is a theoretical method to estimate aggregated fluxes at the surface and the top of the BL from variance profiles (Moeng and Wyngaard 1984). Derivation of vertical profiles of $r_v'^2$ from DIAL data has been attempted by Kiemle *et al.* (1997) and Wulfmeyer (1999). These authors investigated the different sources of measurement errors involved
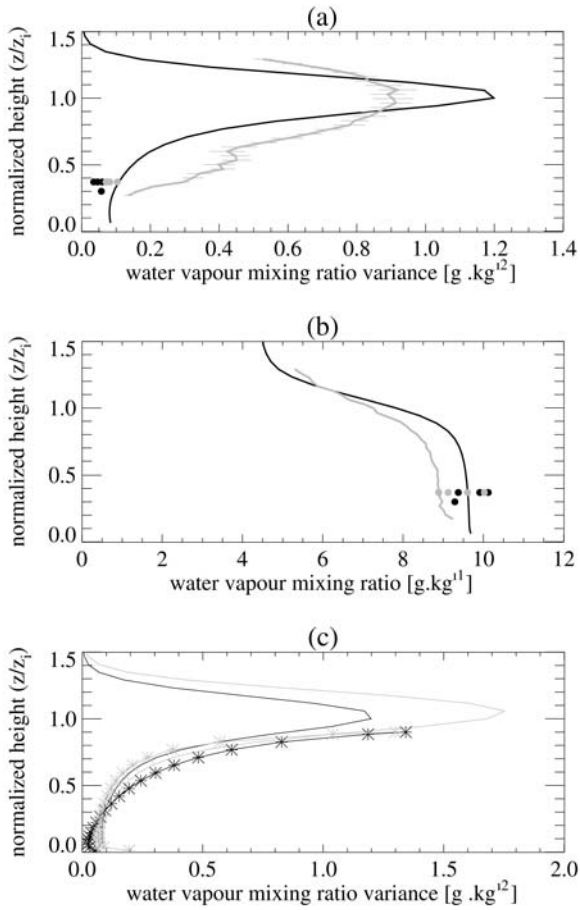
Figure 16. Vertical profiles of water-vapour mixing-ratio derived from three DLR-DIAL measurements during the period 1700–1730 14 June 2002 (grey) and simulated by LES at 1700 UTC at the same, 200 m, vertical resolution (black) (see text for details): (a) variance ($g^2 kg^{-2}$), large dots denote values derived from *in situ* data from the UWKA (grey) and P-3 (black); (b) mean (g kg^{-1}), large dots denote values derived from *in situ* data from the UWKA (grey) and P-3 (black); and (c) variance simulated by LES, total (grey) and contribution from scales larger than 200 m. Stars denote values based on the similarity laws of Moeng and Wyngaard (grey) and Sorbjan (black).

and further compared their estimations to analytic formulations obtained from fits to a few academic LESs (Moeng and Wingaard 1984), with moderate success. In Fig. 16(a) we may compare the vertical profiles of $r_v'^2$ obtained from the airborne DLR DIAL and directly simulated by LES. Three segments of airborne DLR DIAL measurement centred over Homestead are used to compute the variance (in order to reduce the error due to the sampling). They are, in sequence, 10, 10 and 7.5 km long, and were obtained between 1700 and 1730 UTC.

DRL-DIAL derived values of $\overline{r_v'^2}$ at each level are computed after subtracting the white-noise contribution using the method of Lenschow *et al.* (2000). The relative random error arising from the sampling size is less than 20%. Only values computed for levels above 0.3 z_i are plotted since below that level the received signal is dominated by instrumental noise. Variances computed separately from the three segments have

maxima varying from -15% to $+15\%$ relative to their average maximum. The maximum of the simulated $r_v'^2$ profile, located at the BL top, varies during the day. In the simulation, it increases with time until 1700 UTC, i.e. during the significant growth of the BL, and then decreases when the BL grows more slowly. Note that the calculation of the variance on cross-sections parallel to the aircraft leg (instead of over the whole domain) did not change the profile significantly. In Fig. 16(a), the contribution to $r_v'^2$ of scales smaller than 200 m is removed by interpolating the moisture field into the DLR DIAL grid (i.e. 200 m of vertical resolution). This vertical resolution is necessary in order to keep the instrumental noise below 10% in the DIAL data. Note that z_i is determined independently in the LES and in the DIAL observations. It is defined as the altitude where the variance reaches its maximum, as did Wulfmeyer (1999). Variations in the values are noted among observations and simulations but there is obviously a greater correspondence between these 'DIAL' and 'LES-retrieved' profiles than was found by Kiemle *et al.* (1997)—see their Fig. 7. This is possibly related to the relative smallness of the segments considered here. (This smallness efficiently reduces the contribution from mesoscale fluctuations.) The most significant difference between the two estimations is that the peak of the variance is broader in the DIAL data than in the LES, while the maximum associated variance is smaller. Below $0.9 z_i$, DIAL-deduced variance has systematically larger values than the LES. This is consistent with mean r_v values since DIAL r_v vertical profiles suggest a larger transition zone at BL top than LES (Fig. 16(b)). This difference may be for several reasons: higher variability of z_i for DIAL measurements than LES; residual instrumental noise in DIAL data, and an underestimation in the simulation of the dry downdraughts penetrating deep into the CBL[*]. As expected, at the BL top, a systematic correspondence between the strength of vapour gradient and the value of maximum variance is noted both in LES and DIAL measurements, emphasizing the role of entrainment processes in the variance at BL top, with a stronger (weaker) gradient associated with a stronger (weaker) variance.

Figure 16(c) shows vertical profiles of total[†] (resolved plus parametrized subgridscale variance) $r_v'^2$ simulated by the LES at 1700 UTC, and variances resulting from scales larger than 200 m. Both variance profiles are interpolated into the DLR DIAL grid (200 m of vertical resolution). Contributions from scales smaller than 200 m are important between $0.8 z_i$ and $1.2 z_i$, of the order of 30% of the total variance. Moeng and Wyngaard (1984) and Sorbjan (1991)[‡] stated two similarity laws (their Eqs. 3.4 and 9 respectively). The profiles of $r_v'^2$ obtained using their formula are reported in Fig. 16(c). Both laws take into account the entrainment process and involve the ratio of entrainment flux to surface flux for the water-vapour mixing-ratio (R_q). Sorbjan's law also needs the corresponding ratio for potential temperature (R_θ). Here, R_q and R_θ are computed with fluxes from the simulation at 1700 UTC interpolated at 200 m vertical resolution. In the range of R_q and R_θ considered here, they both agree with the total simulated variance. Thus, the neglect of the contribution from smaller scales in the estimation of $r_v'^2$ from DIAL data might also partly explain the differences noted by Kiemle *et al.* (1997) since, in both studies, the LES and the DLR DIAL data have different vertical resolution so that the full variance is not captured by the DIAL measurement. The variance resulting from scales less than 200 m is significant in the upper part of the CBL but is not handled by lidar because of the instrument's vertical resolution.

---

[*] This explanation is consistent with the differences between DIAL and simulated fields of moisture, but not with *in situ* data (shown as dots in Figs. 16(a) and 16(b)) obtained in the middle of the mixed layer.

[†] Only scales smaller than 10 km (the domain size) are represented by the LES.

[‡] $D = 0$ was used for Sorbjan's law.

6. Discussion and conclusions

Moisture fluctuations associated with a growing CBL over land have been investigated by means of LES and observations acquired on 14 June 2002 in the vicinity of Homestead, Oklahoma, USA, in the framework of the IHOP_2002 field-experiment. A composite of early-morning sounding data, together with time series of measured surface-heat-fluxes were used to initialize the LES and prescribe boundary conditions. Large-scale advection deduced from MM5 simulation was also allowed for in the simulation. With this set-up, the LES provides a realistic picture of the BL growth in the morning and early afternoon when compared with balloon soundings, aircraft *in situ* data and observations from lidar. The prescription of large-scale advection significantly improved the simulation.

The observed water-vapour variability exhibits contributions from different scales. Sensitivity tests show that the influence of the mesoscale (>10 km) fluctuations on the submesoscale, assessed using LES and observations, is significant. The observed and simulated variability of θ and r_v in the mixed layer is still large for scales less than 10 km. Mixing is important in the vertical but there are horizontal heterogeneities, as found in previous studies (e.g., Weckwerth *et al*. 1996). The simulated variability is close to the observed, even though surface heat fluxes and initial profiles have been assumed to be horizontally homogeneous. Therefore, to the first order, convective activity in the BL, including entrainment, explains most of the water-vapour variability at submesoscale.

The analysis of horizontal structures indicates that they are characterized by larger scales for water vapour than for potential temperature, which are both larger than for vertical velocity. This result underlines the complexity of the links between convective activity and moisture in the BL. It is also consistent with the studies of Jonker *et al*. (1999) and De Roode *et al*. (2004) based on academic simulations. These studies emphasize the domination of mesoscale fluctuations for scalars for which the entrainment flux is a positive fraction of surface flux even though vertical velocity and potential temperature do not contain such large-scale fluctuations.

In the present case-study, the distributions of w and r_v are both asymmetric in the CBL: the positive skewness of w is consistent with narrow and rapidly ascending thermals, while the negative skewness of r_v reflects the presence of narrow tongues of subsiding dry air originating from the entrainment zone. The latter contrasts with the classical scheme of narrow and rapid thermals and wide slowly subsiding zones. Both mechanisms impact the whole depth of the BL and therefore play an important role in non-local transport (pollutants) and cloud formation. For instance, Zhu and Albrecht (2003) underline the need to sample the thermodynamic properties of the strongest updraughts for an accurate determination of the initiation of fair-weather cumuli. Our results suggest that the departures from the often-assumed 'Gaussianity' of the BL fields might complicate the problem especially for moist convective parametrizations where skewed distributions should therefore be prescribed or diagnosed. Indeed, the skewness of relative humidity in the BL is mostly controlled by the distribution of r_v in the present case (not shown). The positive skewness of the moisture field just above the BL height favours an earlier initiation of clouds than a Gaussian (i.e. 'normal') distribution. In addition, and as noted by Price (2001), observations from this particular case show that, at scales larger than 10 km, mesoscale gradients can also significantly impact the moisture distribution. Indeed, in the present case, the reduction of the skewness found on a scale of $\sim$100 km occurs because of this gradient, which widens the moisture PDF: for this particular day, clouds were first initiated on the moister side

of the area. The strengths of temperature and moisture gradients at BL top can also affect the skewness via modifications of the BL structure. The water-vapour distribution is the result of a complex interaction of convective activity, entrainment, impact of mesoscale processes such as advection or variability in surface fluxes and the prevailing meteorological conditions which arise from the history of the air mass. Knowledge of the vertical and horizontal distribution of water vapour is essential for the determination of the thermodynamic characteristics of the strongest updraughts and cloud properties. In a future study, we plan to analyse the impact of water-vapour variability on moisture fluxes and cumulus clouds initiation and to investigate how the presence of clouds modifies the water-vapour variability.

APPENDIX

Tables 1, 2, 3, 4 and 5 present values as a function of height of the following, respectively: initial profiles; forcing at 1200 UTC; forcing at 1500 UTC; forcing at 1800 UTC and surface fluxes used for the REF simulation. Note that forcing is given at only three times during the simulation period. Linear interpolations between the soundings are computed to get the forcing at other times and a similar forcing is kept after 1800 UTC.

TABLE 1.   INITIAL PROFILES FOR THE LES SIMULATIONS

Height, z (m)	Pot. temp., θ (K)	Wat.-vap. mixing-ratio, r_v (g kg^{-1})	Zonal velocity, u (m s^{-1})	Meridional velocity, v (m s^{-1})
0	296	11.2		
275	299	10.7	0	−0.5
525	300.6	9.6	0	−3
625	301.3	9.1	−1	−3
975	302.6	7.0	−2.7	−4
1125	303	6.1	−3	−5
1325	305	5.1	−2.2	−4.5
1825	307	4.8	1	−5.5
2325	308.2	4.7	2.5	−10
2525	310	4.6	7	−12
3225	314	4.5	16	−8
3475	315	4.5	18.2	−8.7
3675	316	4.0	19.5	−10.5
3775	316.6	3.6	20	−11
4125	318	2.8	19.5	−12
4525	321	1.5	19	−12
4725	323	0.2	19	−12
4975	325.5	0.1	19	−12

TABLE 2. FORCING AT 1200 UTC PRESCRIBED IN THE LES SIMULATIONS

Height z (m)	Zonal wind u (m s^{-1})	Meridional wind v (m s^{-1})	Vertical wind w (m s^{-1})	Hor. advect. of θ (10^{-3}K s^{-1})	Hor. advect. of r_v (10^{-3}g kg^{-1}s^{-1})
15	−0.5	−2.6	0.00	−0.04	−0.02
50	−0.6	−2.7	0.00	−0.04	−0.02
87	−0.9	−2.8	0.00	−0.04	−0.03
123	−1.1	−2.7	0.00	−0.04	−0.03
158	−1.3	−2.7	0.00	−0.03	−0.03
212	−1.5	−2.6	0.00	−0.03	−0.03
285	−1.8	−2.4	−0.005	−0.03	−0.03
358	−2.2	−2.0	−0.01	−0.04	−0.03
431	−2.3	−1.6	−0.01	−0.04	−0.03
505	−2.2	−1.5	−0.01	−0.03	−0.03
580	−2.0	−1.5	−0.01	−0.02	−0.03
655	−1.8	−1.5	−0.01	−0.02	−0.03
769	−1.4	−1.9	−0.01	−0.02	−0.03
923	−0.9	−2.5	−0.01	−0.02	−0.03
1080	−0.6	−3.2	−0.01	−0.02	−0.05
1239	−0.5	−3.9	−0.01	−0.02	−0.06
1401	−1.0	−4.4	−0.01	−0.02	−0.07
1587	−1.9	−5.1	−0.01	−0.02	−0.08
1797	−2.4	−5.8	−0.01	−0.03	−0.09
2122	−1.3	−6.3	−0.01	−0.07	−0.07
2574	2.3	−7.5	−0.01	−0.08	−0.06
3049	6.2	−10.1	−0.01	−0.10	−0.00
3812	12.1	−12.7	−0.005	−0.07	0.00
4500	19.0	−15.0	0.00	−0.05	−0.00

TABLE 3. FORCING AT 1500 UTC PRESCRIBED IN THE LES SIMULATIONS

Height z (m)	u_{forc} (m s^{-1})	v_{forc} (m s^{-1})	w_{forc} (m s^{-1})	Hor. advect. of θ (10^{-3}K s^{-1})	Hor. advect. of r_v (10^{-3}g kg^{-1}s^{-1})
15	−0.9	−2.3	0.00	−0.04	−0.04
50	−0.9	−2.3	0.00	−0.04	−0.04
87	−0.9	−2.3	0.00	−0.04	−0.04
123	−0.9	−2.3	0.00	−0.04	−0.04
158	−0.8	−2.3	0.00	−0.04	−0.04
212	−0.8	−2.3	0.00	−0.04	−0.04
285	−0.8	−2.3	0.00	−0.04	−0.04
358	−0.8	−2.2	0.00	−0.04	−0.04
431	−0.8	−2.2	0.00	−0.04	−0.03
505	−0.8	−2.0	−0.003	−0.04	−0.03
580	−0.7	−1.8	−0.006	−0.03	−0.03
655	−0.5	−1.7	−0.01	−0.03	−0.03
769	−0.0	−1.5	−0.01	−0.02	−0.02
923	0.5	−1.5	−0.01	−0.02	−0.02
1080	0.7	−1.4	−0.01	−0.01	−0.02
1239	0.4	−1.3	−0.01	−0.00	−0.02
1401	−0.1	−1.6	−0.01	−0.01	−0.01
1587	0.1	−2.7	−0.01	−0.03	−0.01
1797	0.9	−4.1	−0.01	−0.04	−0.02
2122	2.3	−5.3	−0.01	−0.05	−0.05
2574	5.0	−6.7	−0.01	−0.06	−0.02
3049	7.3	−9.8	−0.01	−0.10	0.04
3812	12.1	−11.5	−0.005	−0.07	0.01
4500	17.0	−14.0	0.00	−0.05	0.00

TABLE 4.   FORCING AT 1800 UTC PRESCRIBED IN THE LES SIMULATIONS

Height z (m)	u_{forc} (m s^{-1})	v_{forc} (m s^{-1})	w_{forc} (m s^{-1})	Hor. advect. of θ (10^{-3}K s^{-1})	Hor. advect. of r_v (10^{-3}g kg^{-1}s^{-1})
15	−3.8	−0.8	0.00	−0.04	−0.02
50	−3.8	−0.7	0.00	−0.04	−0.02
87	−3.8	−0.7	0.00	−0.04	−0.02
123	−3.8	−0.7	0.00	−0.04	−0.02
158	−3.8	−0.7	0.00	−0.04	−0.02
212	−3.7	−0.6	0.00	−0.04	−0.02
285	−3.7	−0.6	0.00	−0.04	−0.02
358	−3.6	−0.6	0.00	−0.03	−0.02
431	−3.6	−0.5	0.00	−0.03	−0.02
505	−3.5	−0.4	0.00	−0.03	−0.01
580	−3.5	−0.4	−0.001	−0.03	−0.01
655	−3.4	−0.3	−0.002	−0.03	−0.01
769	−3.2	−0.2	−0.004	−0.02	−0.01
923	−2.9	0.1	−0.006	−0.02	−0.00
1080	−2.4	0.4	−0.008	−0.01	0.00
1239	−1.5	0.9	−0.01	0.00	0.01
1401	−0.4	1.5	−0.01	−0.01	0.02
1587	1.3	1.0	−0.01	−0.02	0.06
1797	2.5	−0.8	−0.01	−0.08	0.08
2122	2.7	−2.8	−0.01	−0.03	−0.02
2574	4.4	−4.1	−0.01	−0.04	−0.05
3049	7.4	−5.8	−0.01	−0.11	−0.01
3812	9.9	−10.2	−0.005	−0.08	0.01
4500	13.0	−14.0	0.00	−0.05	0.00

TABLE 5.   SURFACE SENSIBLE- AND LATENT-HEAT FLUX PRESCRIBED IN THE LES SIMULATIONS EVERY HALF HOUR

UTC	Surface sensible-heat flux (W m^{-2})	Surface latent-heat flux (W m^{-2})
1200	5	22
1230	15	44
1300	35	64
1330	60	75
1400	80	87.5
1430	100	100
1500	126	113
1530	137	126
1600	149	135
1630	161	144
1700	172	153
1730	186	161
1800	197	168
1830	209	174
1900	214	179

REFERENCES

Avissar, R. and Schmidt, T.	1998	An evaluation of the scale at which ground-surface heat flux patchiness affects the convective boundary layer using large-eddy simulations. *J. Atmos. Sci.*, **55**, 2666–2689
Bechtold, P., Cuijpers, J. W. M., Mascart, P. and Trouilhet, P.	1995	Modeling of trade wind cumuli with a low-order turbulence model: toward a unified description of Cu and Sc clouds in meteorological models. *J. Atmos. Sci.*, **52**, 455–463
Berg, L. K. and Stull, R. B.	2004	Parameterization of joint frequency distributions of potential temperature and water vapour mixing ratio in the daytime convective boundary layer. *J. Atmos. Sci.*, **61**, 813–828
Brown, A. R., Cederwall, R. T., Chlond, A., Duynkerke, P. G., Golaz, J.-C., Khairoutdinov, M., Lewellen, D. C., Lock, A. P., MacVean, M. K., Moeng, C.-H., Neggers, R. A. J., Siebesma, A. P. and Stevens, B.	2002	Large-eddy simulation of the diurnal cycle of shallow cumulus convection over land. *Q. J. R. Meteorol. Soc.*, **128**, 1075–1093
Couvreux, F., Weckwerth T. M. and Pinto, J.	2002	'Assimilation des données de l'interféromètre AERI dans MM5'. In proceedings of Ateliers de Modélisation de l'Atmosphère (AMA), 17–19 December 2002, Toulouse, France. Available from fleur.couvreux@meteo.fr
Crook, N. A.	1996	Sensitivity of moist convection forced by boundary-layer processes to low-level thermodynamic fields. *Mon. Weather Rev.*, **124**, 1767–1785
Crum, T. D. and Stull, R. B.	1987	Field measurements of the amount of surface layer air versus height in the entrainment zone. *J. Atmos. Sci.*, **44**, 2743–2753
Cuxart, J., Bougeault, P. and Redelsperger, J.-L.	2000	A turbulence scheme allowing for mesoscale and large-eddy simulations. *Q. J. R. Meteorol. Soc.*, **126**, 1–30
Deardorff, J. W.	1972	Numerical investigation of neutral and unstable planetary boundary layers. *J. Atmos. Sci.*, **29**, 91–115
Ehret, G., Hoinka, K. P., Stein, J., Fix, A., Kiemle, C. and Poberaj, G.	1999	Low stratospheric water vapour measured by an airborne DIAL. *J. Geophys. Res.*, **104**, 31351–31359
Fedorovich, E., Conzemius, R. and Mironov, D.	2004	Convective entrainment into shear-free, linearly stratified atmosphere: bulk models re-evaluated through large eddy simulations. *J. Atmos. Sci.*, **61**, 281–295
Flamant, C., Guichard, F., Van Baelen, J., Bock, O., Couvreux, F., Parsons, D., Weckwerth, T., Pelon, J., Drobinski, P., Lhomme, K., Guenno M. and Doerflinger, E.	2003	La campagne IHOP 2002 : une campagne de mesure de la vapeur d'eau dans la couche limite. *La Météorologie*, **43**, 38–47
Grell, G. A., Dudhia, J. and Stauffer, D. R.	1995	'A description of the fifth generation Penn State/NCAR mesoscale model (MM5)'. *NCAR Technical Note* NCAR/TN-398+1A, National Center for Atmospheric Research, Boulder, CO, USA. Available from NTIS, Springfield, VA, USA
Hechtel, L. M., Moeng, C.-H. and Stull, R. B.	1990	The effects of nonhomogeneous surface fluxes on the convective boundary layer: a case-study using large eddy simulation. *J. Atmos. Sci.*, **47**, 1721–1741
Jonker, H. J. J., Duynkerke, P. G. and Cuijpers, J. W.	1999	Mesoscale fluctuations in scalars generated by boundary layer convection. *J. Atmos. Sci.*, **56**, 801–808
Kiemle, C., Ehret, G., Giez, A., Davis, K. J., Lenschow, D. H. and Oncley, S. P.	1997	Estimation of boundary-layer humidity fluxes and statistics from airborne differential absorption lidar (DIAL). *J. Geophys. Res.*, **102**, 29189–29203
Lafore, J.-P., Stein, J., Asencio, N., Bougeault, P., Ducrocq, V., Duron, J., Fischer, C., Héreil, P., Mascart, P., Masson, V., Pinty, J. P., Redelsperger, J.-L., Richard, E. and Vila-Guerau de Arellano, J.	1998	The Meso-NH atmospheric simulation system. Part I: adiabatic formulation and control simulations. *Ann. Geophys.*, **16**, 90–109

Larson, V. E., Wood, R., Field, P. R., Golaz, J.-C., Vonder Haar, T. H. and Cotton, W. R.	2001	Small-scale and mesoscale variability of scalars in cloudy boundary layers: one-dimensional probability density functions. *J. Atmos. Sci.*, **58,** 1978–1994
Lemone, M. A.	1990	Some observations of vertical velocity skewness in the convective planetary boundary layer. *J. Atmos. Sci.*, **47,** 1163–1169
Lenschow, D. H. and Stankov, B. B.	1986	Length-scales in the convective boundary layer. *J. Atmos. Sci.*, **43,** 1198–1209
Lenschow, D. H., Wulfmeyer, V. and Senff, C.	2000	Measuring second- through fourth-order moments in noisy data, *J. Atmos. Oceanic Technol.*, **17,** 1330–1347
Letzel, M. O. and Raasch, S.	2003	Large Eddy Simulation of Thermally Induced Oscillations in the Convective Boundary Layer. *J. Atmos. Sci.*, **60,** 2328–2341
Lohou, F., Druilhet, A., Campistron, B., Redelsperger, J.-L. and Saïd, F.	2000	Numerical study of the impact of coherent structures on vertical transfers in the atmospheric boundary layer. *Boundary-Layer Meteorol.*, **97,** 361–383
Mace, G. G. and Ackerman, T. P.	1996	Assessment of error in synoptic-scale diagnostics derived from wind profiler and radiosonde network data. *Mon. Weather Rev.*, **124,** 1521–1534
Mahrt, L.	1991	Boundary-layer moisture regimes. *Q. J. R. Meteorol. Soc.*, **117,** 151–176
Mason, P. J.	1989	Large-eddy simulation of the convective atmospheric boundary layer. *J. Atmos. Sci.*, **46,** 1492–1516
Moeng, C.-H.	1984	A large-eddy simulation model for the study of planetary boundary-layer turbulence. *J. Atmos. Sci.*, **41,** 2052–2062
Moeng, C.-H. and Sullivan, P. P.	1994	A comparison of shear- and buoyancy-driven planetary-boundary-layer flows. *J. Atmos. Sci.*, **51,** 999–1022
Moeng, C.-H. and Wyngaard, J. C.	1984	Statistics of conservative scalars in the convective boundary layer. *J. Atmos. Sci.*, **41,** 3161–3169
Price, J. D.	2001	A study of probability distributions of boundary-layer humidity and associated errors in parametrized cloud-fraction. *Q. J. R. Meteorol. Soc.*, **127,** 739–758
Redelsperger, J.-L. and Sommeria, G.	1982	Method of representing the turbulence associated with precipitations in a three-dimensional model of cloud convection. *Boundary-Layer Meteorol.*, **24,** 231–252
	1986	Three-dimensional simulation of a convective storm: sensitivity studies on subgrid parameterization and spatial resolution. *J. Atmos. Sci.*, **43,** 2619–2635
De Roode, S., Duynkerke, P. G. and Jonker, H. J.	2004	Large Eddy Simulation: How large is large enough? *J. Atmos. Sci.*, **61,** 403–421
Schmidt, H. and Schumann, U.	1989	Coherent structure of the convective boundary layer derived from large-eddy simulations. *J. Fluid Mech.*, **200,** 511–562
Sorbjan, Z.	1991	Evaluation of local similarity functions in the convective boundary layer. *J. Appl. Meteorol.*, **30,** 1565–1583
Stull, R. B.	1985	A fair-weather cumulus cloud classification scheme for mixed layer studies. *J. Appl. Meteorol.*, **24,** 49–56
Sullivan, P., Moeng, C.-H., Stevens, B., Lenschow D. H. and Mayor, S. D.	1998	Structure of the entrainment zone capping the convective atmospheric boundary layer. *J. Atmos. Sci.*, **55,** 3042–3064
Tennekes, H.	1973	A model for the dynamics of the inversion above a convective boundary layer. *J. Atmos. Sci.*, **30,** 558–567
Wang, J., Cole, H. L., Carlson, D. J., Miller, E. R., Beierle, K., Paukkunen, A. and Laine, T. K.	2002	Corrections of humidity measurement errors from the Vaisala RS80 radiosonde—Application to TOGA COARE data. *J. Atmos. Oceanic Technol.*, **19,** 981–1002
Weckwerth, T. M.	2000	The effect of small-scale moisture variability on thunderstorm initiation. *Mon. Weather Rev.*, **128,** 4017–4030
Weckwerth, T. M., Wilson, J. W. and Wakimoto, R. M.	1996	Thermodynamic variability within the convective boundary layer due to horizontal convective rolls. *Mon. Weather Rev.*, **124,** 769–784
Weckwerth, T. M., Wulfmeyer, V., Wakimoto, R. M., Hardesty, R. M., Wilson, J. W. and Banta, R. M.	1999	NCAR–NOAA Lower tropospheric water vapour workshop. *Bull. Am. Meteorol. Soc.*, **80,** 2339–2357

Weckwerth, T. M., Parsons, D. B.,   2004   An overview of the International H20 Project (IHOP_2002) and
    Koch, S. E., Moore, J. A.,   some preliminary highlights. *Bull. Am. Meteorol. Soc.*, **85,**
    Lemone, M. A., Demoz, B. R.,   253–277
    Flamant, C., Geerts, B.,
    Wang, J. and Feltz, W.
Wilde, N. P., Stull, R. B. and   1985   The LCL zone and cumulus onset. *J. Clim. Appl. Meteorol.*, **24,**
    Eloranta, E. W.   640–657
Wulfmeyer, V.   1999   Investigations of humidity skewness and variance profiles in the
                                             convective boundary layer and comparison of the latter with
                                             large eddy simulation results. *J. Atmos. Sci.*, **56,** 1077–1087
Wyngaard, J. C., Pennell, W. T.,   1978   The temperature–humidity covariance budget in the convective
    Lenschow, D. H. and   boundary layer. *J. Atmos. Sci.*, **35,** 47–58
    LeMone, M. A.
Zhu, P. and Albrecht, B.   2002   A theoretical and observational analysis on the formation of
                                             fair-weather cumuli. *J. Atmos. Sci.*, **59,** 1983–2005
                                      2003   Large eddy simulations of continental shallow cumulus
                                             convection. *J. Geophys. Res.*, **108**(D15)**,** 4453